

# **Report to the Grant AOARD-08-4049**

## **Development of High ZT Thermoelectric Materials With Nanostructure For Energy Applications**

### **Principal Investigator:**

**Maw-Kuen Wu, Institute of Physics, Academia Sinica, Taiwan**

### **Co-Investigator:**

**Yang-Yuan Chen, Institute of Physics, Academia Sinica**

### **I. Background and motivation:**

Thermoelectricity was first observed in 1823 by Seebeck, who found that a current would flow in a closed circuit made of two dissimilar metals when the two junctions were maintained at different temperatures. Twelve years later, a reverse effect was discovered by Peltier, who observed temperature changes in the vicinity of the junction between dissimilar conductors when a current was passed through the junction. In 1851 W. Thomson established a relationship between the Seebeck coefficient ( $S$ ) and Peltier coefficient ( $\Pi$ ) and predicted the existence of a third thermoelectric effect, the Thomson effect, which he subsequently observed experimentally. Since then much work has been done to make use of thermoelectric physics. Thermoelectric materials have the advantage of no mechanical parts, no need for coolant to operate, quiet performance, and can be utilized as a heat-electricity converter. Therefore, thermoelectric materials can be used either as a power generator based on the Seebeck effect, or as a thermo-cooler based on the Peltier effect. The current state-of-the-art thermoelectric materials commercially used for refrigeration and power generation are  $\text{Bi}_2\text{Te}_3$  with  $T$  down to about 250 K and  $\text{Si}_{1-x}\text{Ge}_x$  with  $T > 700$  K.

### **II. The efficiency of thermoelectric materials- figure of merit ZT:**

The efficiency of thermoelectric materials is determined by the dimensionless figure of merit ZT

$$ZT = S^2 \sigma T / (\kappa_e + \kappa_l),$$

where  $S$  is the Seebeck coefficient ( $S = \Delta V / \Delta T$ ),  $\sigma$  is the electrical conductivity,  $\kappa_e$  is the thermal conductivity of electrons, and  $\kappa_l$  is the thermal conductivity of lattice phonons. Good thermoelectric materials should possess a large Seebeck coefficient, low thermal conductivity  $\kappa_e + \kappa_l$ , and high electrical conductivity. This concept is related to Slack's earlier proposal of a "Phonon-Glass/Electron-Crystal" (PGEC) model, which suggests that a good thermoelectric material should have the electronic properties of a crystalline material and the thermal properties of a glass. Applications only become practical for  $ZT > 2$ , and at a ZT of 3, thermoelectric materials would become competitive with vapor-compression refrigeration systems. It has been a challenge to increase  $ZT > 1$  since the parameters,  $S$ ,  $\sigma$  and  $\kappa$ , are generally interdependent.

By properly adjusting the parameters of  $S$ ,  $\sigma$  and  $\kappa$ , the figure of merit ZT can possibly be enhanced. According to *Weideman-Franz law*,  $\sigma T / \kappa_e = 3(k/e)^2 / \pi^2 = 1 / (156 \mu\text{V/K})^2$  is a constant. This means that in general, increasing the electrical conductivity  $\sigma$  will increase  $\kappa_e$  proportionally. We ignore the lattice thermal conductivity,  $\kappa_l$ , as it can be reduced by increasing phonon scattering.

### **Proposed Works**

There are three topics proposed as the core researches in this proposal. In the following we describe, respectively, our research results on the proposed topics.

### **Research approach A—Investigate the systems of “surface modified nanostructured bulk”**

Report Documentation Page				Form Approved OMB No. 0704-0188	
Public reporting burden for the collection of information is estimated to average 1 hour per response, including the time for reviewing instructions, searching existing data sources, gathering and maintaining the data needed, and completing and reviewing the collection of information. Send comments regarding this burden estimate or any other aspect of this collection of information, including suggestions for reducing this burden, to Washington Headquarters Services, Directorate for Information Operations and Reports, 1215 Jefferson Davis Highway, Suite 1204, Arlington VA 22202-4302. Respondents should be aware that notwithstanding any other provision of law, no person shall be subject to a penalty for failing to comply with a collection of information if it does not display a currently valid OMB control number.					
1. REPORT DATE <b>03 MAR 2010</b>		2. REPORT TYPE <b>Final</b>		3. DATES COVERED <b>25-03-2008 to 05-03-2010</b>	
4. TITLE AND SUBTITLE <b>Development of High ZT Thermoelectric Materials with Nanostructure for Energy Applications</b>				5a. CONTRACT NUMBER <b>FA48690814049</b>	
				5b. GRANT NUMBER	
				5c. PROGRAM ELEMENT NUMBER	
6. AUTHOR(S) <b>Maw-Kuen Wu</b>				5d. PROJECT NUMBER	
				5e. TASK NUMBER	
				5f. WORK UNIT NUMBER	
7. PERFORMING ORGANIZATION NAME(S) AND ADDRESS(ES) <b>Academia Sinica,128 Academia Rd., Section 2,Nankang,Taipei ,TW,11529</b>				8. PERFORMING ORGANIZATION REPORT NUMBER <b>N/A</b>	
9. SPONSORING/MONITORING AGENCY NAME(S) AND ADDRESS(ES) <b>Asian Office of Aerospace Research &amp; Development, \(\text{AOARD}\), Unit 45002, APO, AP, 96338-5002</b>				10. SPONSOR/MONITOR'S ACRONYM(S) <b>AOARD</b>	
				11. SPONSOR/MONITOR'S REPORT NUMBER(S) <b>AOARD-084049</b>	
12. DISTRIBUTION/AVAILABILITY STATEMENT <b>Approved for public release; distribution unlimited</b>					
13. SUPPLEMENTARY NOTES					
14. ABSTRACT Three subtasks were performed in this research study and the respective findings are described here. A?Investigation of the system of surface modified nanostructured bulk: Our studies show that the CuFeSe2 thin film on Si (or SiO2) substrates exhibit large thermal power in the order of 1300 microvolt/K at ~300K. We conclude that the thinner films have the higher thermal conductivity. At 300K, the magnitude of thermal conductivity 8.8 W/m-K for 200 nm is about two times larger than 1.7 W/m-K of the 800 nm film. The consequence is attributed to the better crystallization in thinner films. This film thickness dependence of crystallization was confirmed by X-ray diffraction data. In this report, the thermal resistance of the interface boundaries in SiNx-CuFeSe2 was estimated to be 3.32?0-8 Km2/W. We cannot give a clear estimate of the ZT value for these films at the moment. The major difficulty came from the exact value of the thermoelectric power of the thin film. B?Investigation of one-dimensional nanowires: Bismuth telluride film and nanowires array (embedded in alumina template) were fabricated by potentiostatically electrodeposition. The Seebeck coefficient, electrical resistivity and thermal conductivity of a single nanowire provide an estimated thermoelectric figure of merit $ZT = 0.45$ at 300 K and likely to reach beyond 0.9 above 350 K, for Bi2Te3 nanowires. C?Directional dependent thermal conductivity and thermal rectifier: we cannot make a conclusive statement that there exists no rectification effect, as the narrowest section in our device is still too big compared with that observed in carbon and boron nitride nanotubes.					
15. SUBJECT TERMS <b>Nanotechnology, Thermoelectric, Figure of merit ZT</b>					
16. SECURITY CLASSIFICATION OF:			17. LIMITATION OF ABSTRACT <b>Same as Report (SAR)</b>	18. NUMBER OF PAGES <b>18</b>	19a. NAME OF RESPONSIBLE PERSON
a. REPORT <b>unclassified</b>	b. ABSTRACT <b>unclassified</b>	c. THIS PAGE <b>unclassified</b>			

In this particular topics, we have put our focus on the investigation of a newly synthesized materials,  $\text{CuFeSe}_2$ , which has a layer-like structure. In addition, it also exhibit an interesting magnetic characteristic originates from the Fe-Se layer. Therefore, we have carried out an extensive study on the the preparation and characterization of  $\text{CuFeSe}_2$  compound, in particular the material in thin film form.

$\text{CuFeSe}_2$  is a type I-III-VI<sub>2</sub> semiconductor with direct band gap 0.16 eV [1]. It has a tetragonal structure, with space group  $P-42c$  and lattice constants  $a = 5.53 \text{ \AA}$ ,  $c = 11.049 \text{ \AA}$  [2]. It is considered to be the small band gap photoelectric material [3-6]. For semiconductor applications the thermal properties of thin film are important parameters. We used the pulse laser ablation (PLA) to grow high quality  $\text{CuFeSe}_2$  thin film on silicon oxide substrate, and use X-ray diffraction to determine the its structure and quality. The result shows that the thin films have highly preferred orientation. Here we applied the differential  $3\omega$  technique to the measurement of thermal conductivity for different thickness thin film specimens, to extract the thermal boundary contribution and the intrinsic thermal conductivity of the thin films.

### A1. Sample preparation

Thin films were grown by laser ablation from a target with the composition  $\text{Cu:Fe:Se} = 1:1:2$ , the target is 25.4 mm in diameter and 8 mm in thickness. The target was sintered at  $600 \sim 700 \text{ }^\circ\text{C}$  under vacuum. After sintering, the target was mechanical polished before each deposition process in order to keep the consistence and the reproducibility for successive deposition processes. Thin films were deposited in vacuum of  $10^{-5}$  Torr. A KrF excimer laser with  $\lambda = 248 \text{ nm}$  (Lambda Physik LPX Pro) was chosen as the ablation source. The laser beam was scanned on the surface of target with pulse frequency of 5 Hz. The scanning area is a  $10 \times 4 \text{ mm}^2$  rectangle. The laser power is  $5 \sim 6 \text{ J/cm}^2$ . The distance between the target and the substrate is around 4.5 to 5.0 cm. In this work, thin films were deposited on  $12 \times 12 \text{ mm}^2$  Si wafer (1 0 0) substrates with 400 nm  $\text{SiO}_2$  surface layer at  $250 \text{ }^\circ\text{C}$ . Before the deposition, the substrates were ultrasonically cleaned in methanol, isopropanol, acetone, and then fixed by silver paint on the stainless steel holder. For differential  $3\omega$  measurement purpose, the thin films was deposited on one half of the substrate with the rest half for reference.

On top of the  $\text{CuFeSe}_2$  film a 300 nm  $\text{SiN}_x$  thin layer was then deposited using plasma-enhanced chemical vapor deposition (PECVD) to serve as an insulation layer for the later deposited Au-Cr strip. We chose  $\text{SiN}_x$  for the insulation layer because of its good thermal conductivity. The Au-Cr strip was first thermal deposited a 10 nm Cr film then followed by a 150 nm Au film, the width and the length of the Au-Cr microprobe is  $4 \text{ }\mu\text{m}$  and 1.5 mm respectively. There are two microprobes, one on the thin film and the other on the substrate (Fig. A1). With these two microprobes the temperature drop across the thin film can be measured, and the thermal conductivity can be derived afterwards.

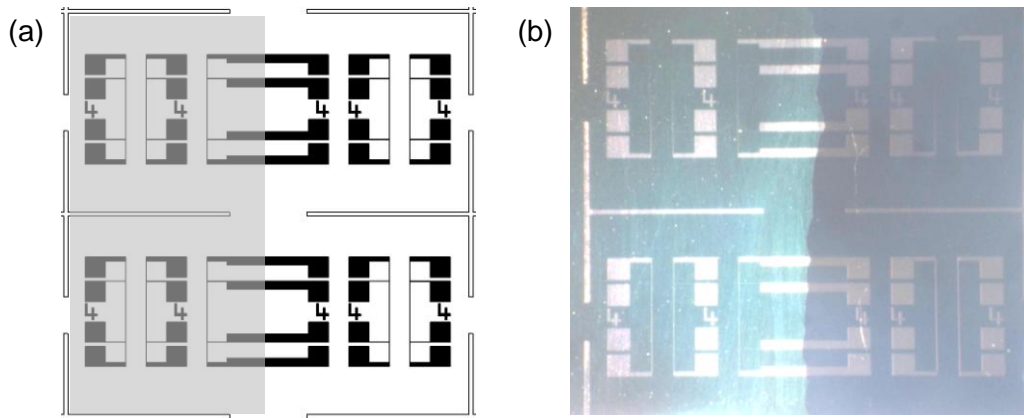


**Fig. A1** (a) The schematic diagram shows the microprobe pattern, the gray side represents the film deposited (b) The corresponding specimen, in which  $\text{CuFeSe}_2$  film was deposited in the left half (the bright part), the right half is the reference without film deposited.

## A2. Structural characterization

The  $\text{CuFeSe}_2$  films were characterized by X-rays diffraction using a PANalytical X'Pert PRO MPD system with copper anode ceramic tube as source and multi channels X'Celerator as detector. The theta-2theta measurement results are shown in Fig. A2. The preferred orientation in (h 0 0) planes was clearly reflected in (200), (400), and (600) peaks. This means the crystalline in the films are highly aligned, and with a-b plane perpendicular to the substrate surface. Particularly a small peak of  $\text{CuFeSe}_2$  (112) starts to grow for 400 nm film.

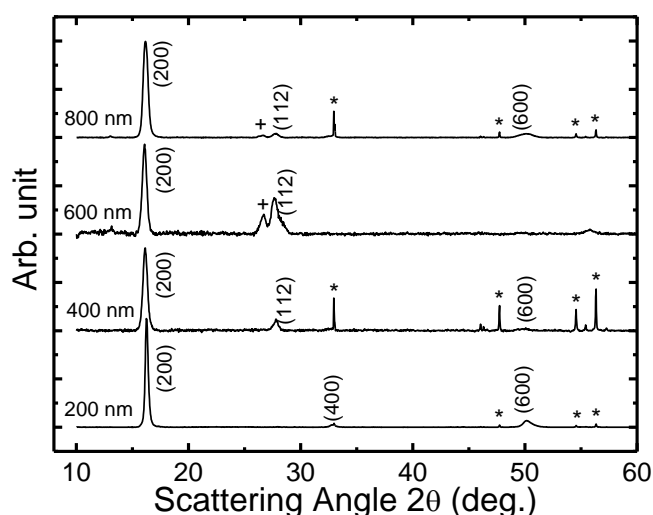


**Fig. A2** The x-ray diffraction for 200, 400, 600 and 800 nm films.

The planes of (200), (400), and (600) are clearly observed in 200 and 400 nm films. The mark \* represents the peak of  $\text{SiO}_2$  substrate. The mark + represent the second phase  $\text{Cu}_2\text{Se}$  (111) peak in 600 and 800 nm films. It shows the 800 nm and 600 nm thin films have larger d-spacing and orientation distribution.

The similar result was also shown in the rocking curve measurement data (Fig. A3). The rocking curve of (200) plane ( $2\theta=16.104^\circ$ ) were measured for 200 nm, 600 nm, and 800 nm films. It is very clear that 800 nm and 600 nm sample have the broader width than 200 nm sample. Although the thicker  $\text{CuFeSe}_2$  film has preferred orientation in (200) but the orientation of the crystalline is not as fine as it in 200 nm sample. This explains why the lower cross plane thermal conductivity in thicker films.

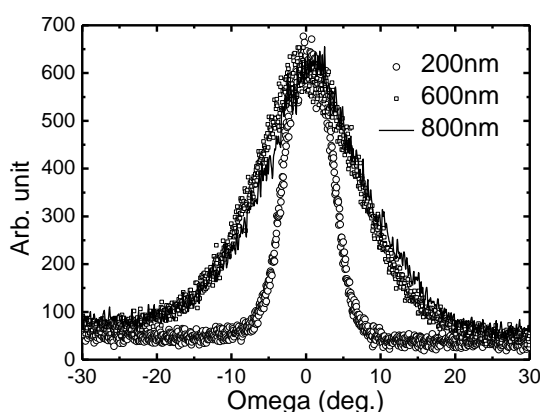


**Fig. A3** The rocking curve profile for 200, 600, and 800 nm sample. The 200 nm sample has the thinner width of half maximum than thicker samples.

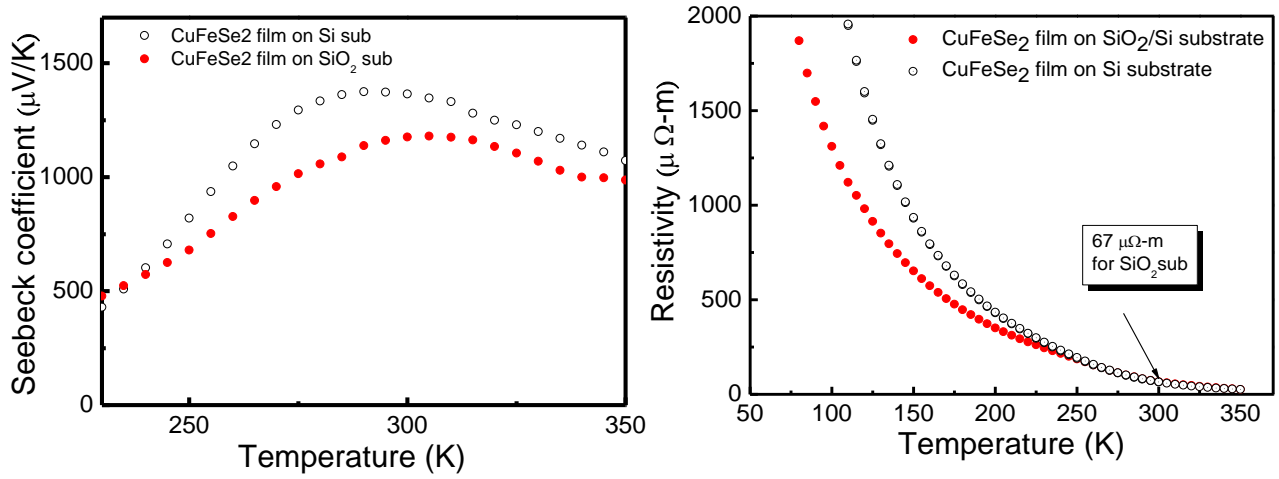


**Figure A4.** Temperature dependence of Seebeck coefficient (left panel) and electrical resistivity (right panel) of CuFeSe<sub>2</sub> thin films (on both Si and SiO<sub>2</sub> substrates).

### A3. $3\omega$ technique for thin film

The thermoelectric power and electrical resistivity of the deposited film are shown in Figure A4. The thermoelectric power of this material shows a broad maximum at around 300 K. The value is unexpectedly high on either Si or SiO<sub>2</sub> substrates. On the other hand, a strong semiconductor-like resistivity was observed in these materials. The most difficult part in this study is to determine the thermal conductivity of the films. The followings are the results of our study.

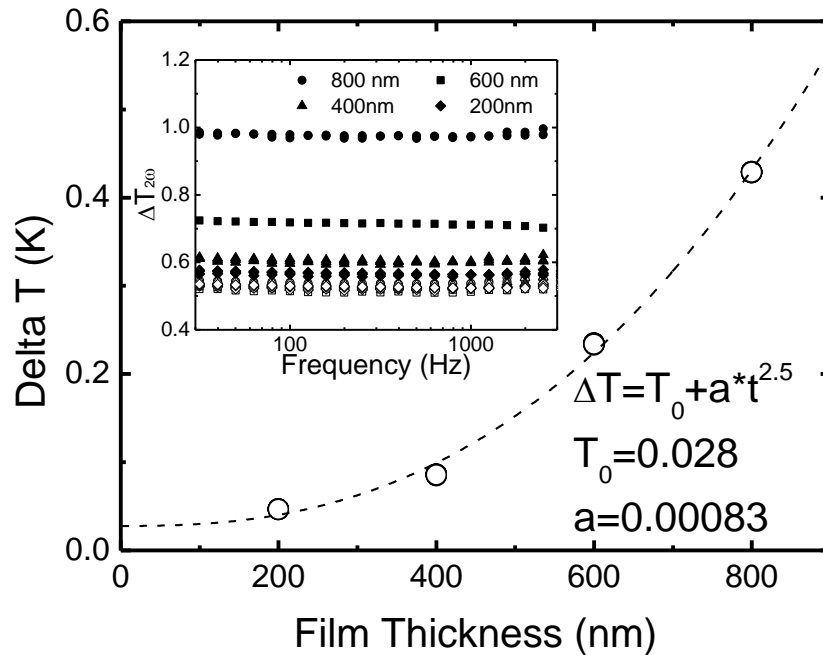


**Fig. A5** The thickness dependence of temperature drop across film. Inset: The solid and open symbols represent the temperatures of top and bottom surfaces of films respectively at 300 K.

The thermal conductivity across films was measured by differential  $3\omega$  technique [7,8]. A strip consisting layers of 150 nm Au and 10 nm Cr with 4  $\mu\text{m}$  width and 1.5 mm length is deposited as the microprobe by photolithography. The microprobe was driven by an AC power  $P$  at frequency  $\omega$ . The resulting third-harmonic voltage was measured by a lock-in amplifier. The  $3\omega$  signals both on thin film

and reference part are converted to AC temperature variation. The difference between two microprobes is the temperature drop across CuFeSe<sub>2</sub> thin film, which is used to calculate the cross plane thermal conductivity.

The temperature drop of different thickness film was shown in Fig. A5. By the thickness dependence of temperature drop, it is clearly seen that the thicker film samples of 600 and 800 nm, have higher temperature drop which is attributed to the structural disorders in films. This result is consistent with the conclusion of X-ray data, i.e. the thinner films have better crystallization in structure. A more detailed analysis of the temperature drop shows it fits to the equation  $\Delta T = \Delta T_0 + a t^n$ , where  $t$  represents the film thickness. The thermal resistance  $K_B$  of the interface boundaries was estimated as  $3.32 \times 10^{-8}$  K-m<sup>2</sup>/W from  $P/\Delta T_0$ . Applying this result to all films, the thermal conductivity of all the films was obtained and plotted in Fig. A6 and A7. Basically the thermal conductivity is approximately linear on temperature. One interesting finding is that the thinner of the film the larger the thermal conductivity. For example, at 300 K the thermal conductivity of 200, 400, 600 and 800 nm films are 8.8, 5.7, 2.4, and 1.7 W/m-K respectively. This consequence is attributed to the condition of crystallization which was confirmed by X-ray diffraction data Fig. A3.

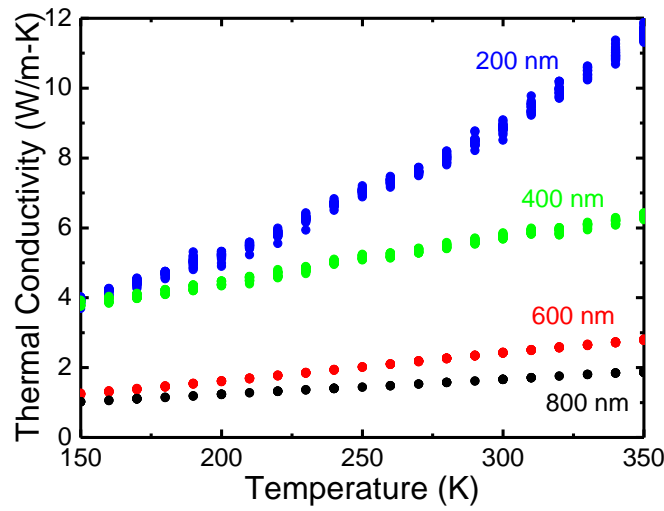


**Fig. A6** Temperature dependence of thermal conductivity of 200, 400 , 600, and 800 nm CuFeSe<sub>2</sub> thin films.

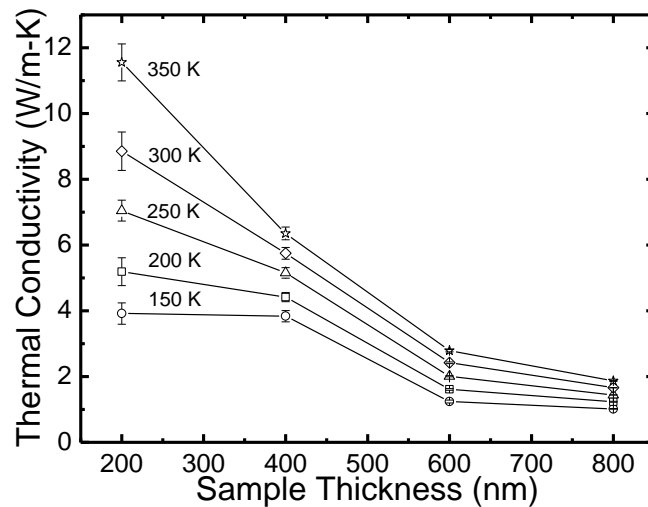


**Fig. A7** The thickness dependence of thermal conductivity at various temperatures.

The inset in Fig A5 shows the original data of frequency dependence of temperature variation  $\Delta T_{2\omega}$  of sample and reference respectively. Their difference is the temperature drop  $\Delta T$  across the film. The thermal conductivity of Si substrate was calculated from the slope of  $\Delta T_{2\omega}$  vs. frequency. [7]. The result is consistent with that reported in literature.

#### A4. Summary of our results

Our studies show that the CuFeSe<sub>2</sub> thin film on Si (or SiO<sub>2</sub>) substrates exhibit large thermal power in the order of 1300  $\mu\text{V/K}$  at  $\sim 300\text{K}$ . However, it decreases rapidly as temperature drops. Unfortunately, we do not have the setup for measurement at temperature above 350K. It will be interesting to find out how it behaves at this elevated temperature. On the other hand, the electrical resistivity shows typical semiconductor-like behavior with a value close to 67  $\mu\Omega\text{-m}$  at 300K. We also obtained the thermal conductivity of the CuFeSe<sub>2</sub> thin film on silicon oxide substrate. We conclude that the thinner films have the higher thermal conductivity. At 300K, the magnitude of thermal conductivity 8.8 W/m-K for 200 nm is about two times larger than 1.7 W/m-K of the 800 nm film. The consequence is attributed to the better crystallization in thinner films. This film thickness dependence of crystallization was confirmed by X-ray diffraction data. In this report, the thermal resistance of the interface boundaries in SiN<sub>x</sub>-CuFeSe<sub>2</sub> was estimated to be  $3.32 \times 10^{-8} \text{ Km}^2/\text{W}$ . We can not give a clear estimate of the ZT value for these films at the moment. The major difficulty came from the exact value of the thermoelectric power of the thin film. Our measurements give only the results of the films plus the contributions from the substrate. We have the difficulty to separate these two contributions with our current experimental set-up.

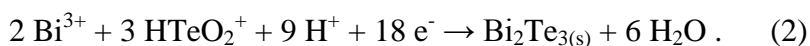
#### Research approach B—Investigate one-dimensional nanowires

The Si nanowires of 9-20 nm and 50-200 nm investigated by Boukai et al and Hochbaum et al, respectively, showed smaller thermal conductivity, larger Seebeck coefficient and an enhancement of  $ZT \sim 1$  at room temperature. The 100-fold improvement over bulk Si is really a breakthrough in thermoelectric nanowires. Intrinsic Bi<sub>2</sub>Te<sub>3</sub> bulk is n-type with  $S \sim 250 \mu\text{V/K}$ , whereas bulk Sb<sub>2</sub>Te<sub>3</sub> is p-type with  $S = 100 \mu\text{V/K}$ . Our preliminary studies on Bi<sub>2</sub>Te<sub>3</sub> and Sb<sub>2</sub>Te<sub>3</sub> nanowire arrays in anodized alumina template revealed that the Seebeck coefficients are 60  $\mu\text{V/K}$  for 50 nm Bi<sub>2</sub>Te<sub>3</sub> and 160  $\mu\text{V/K}$  for 70 nm Sb<sub>2</sub>Te<sub>3</sub> nanowire arrays. The Seebeck coefficient of the former is smaller than its bulk, whereas the latter shows opposite result with Seebeck coefficient larger than the bulk. The size effects on the two systems are quite different and should be further investigated.

To elucidate low-dimensional effects on thermoelectric materials, with the support of this grant, we further investigated the bismuth telluride film and nanowires array, which were fabricated by potentiostatically electrodeposition. The followings are our reports on the synthesis and characterizations of these nano-materials.

#### B1. Synthesis of the nanomaterials

Bi<sub>2</sub>Te<sub>3</sub> films were electrodeposited potentiostatically at -150 mV onto an ITO glass substrate from 1 M HNO<sub>3</sub> solution containing 0.008 M Bi<sup>3+</sup> and 0.014 M HTeO<sub>2</sub><sup>+</sup>. The overall chemical reaction can be described as [9]



The process was carried out in a conventional three-electrode cell with a saturated calomel electrode as the reference and a platinum sheet as the counter electrode. To remove oxygen from solution, argon was bubbled into the electrolyte throughout the experiment. After electrodeposition, as-prepared Bi<sub>2</sub>Te<sub>3</sub> films were annealed in argon with 5 % H<sub>2</sub> at 523 K for 2 hours.

The AAM template was produced in a two-step anodized process [10]. An aluminum foil with purity 99.999 % and thickness 0.13 mm (Alfa Aesar) was anodized in acid solutions, yielding an array of densely packed, hexagonally arranged, parallel nanochannels. The channel diameter can be

systematically controlled by anodized voltage, type of electrolyte and bath temperature. After anodization, the remaining aluminum layer was removed by  $\text{CuCl}_2$  solution. A subsequent etching treatment by 0.5M NaOH aqueous solution for 7~10 min was carried out to remove the barrier layer on the bottom side, followed by depositing a gold-film layer to serve as conductive electrode.

By filling the template, a  $\text{Bi}_2\text{Te}_3$  nanowires array was then fabricated with similar growth conditions, rinsed with deionized water and dried in nitrogen. A thin gold film (~300 nm) was thermally evaporated onto the top surface for oxidation prevention. It was suggested that annealing treatment to nanowires would improve their thermoelectric properties [11]. Our experience indicated that annealing does lower electrical resistivity of as-prepared film as expected, but the annealing-induced thermal shock leads to extremely high electrical resistance in nanowires embedded in AAM. Therefore, experimental data and analysis were confined to  $\text{Bi}_2\text{Te}_3$  bulk, annealed films and as-prepared nanowires. To obtain individual nanowires, AAM was dissolved in 2 M NaOH aqueous solution, then washed by deionized water and centrifuged to remove residual NaOH thoroughly. Separated  $\text{Bi}_2\text{Te}_3$  nanowires were dispersed in ethanol, ready for measurements.

For comparison with films and nanowires, a  $\text{Bi}_2\text{Te}_3$  bulk was prepared by Bridgeman method. Briefly, high-purity (99.999 %) bismuth and tellurium powers were mixed in the appropriate molar ratio and sealed in a quartz tube, which was evacuated to  $10^{-5}$  torr, kept in a furnace at 1073 K for 12 hours, and then cooled down to room temperature in one day.

## B2. Structure characterizations

A 3-KW diffractometer (Philips) equipped with an array detector based on real time multiple strip was employed for crystal structural characterization. Morphologies of films and nanowires array were determined by a field emission scanning electron microscope (SEM, Hitachi S-4200), and compositions by energy dispersive X-ray. Transmission electron micrographs (TEM) and diffraction patterns were obtained with a field emission transmission electron microscope operated at 200 kV (JEOL JEM-2100).

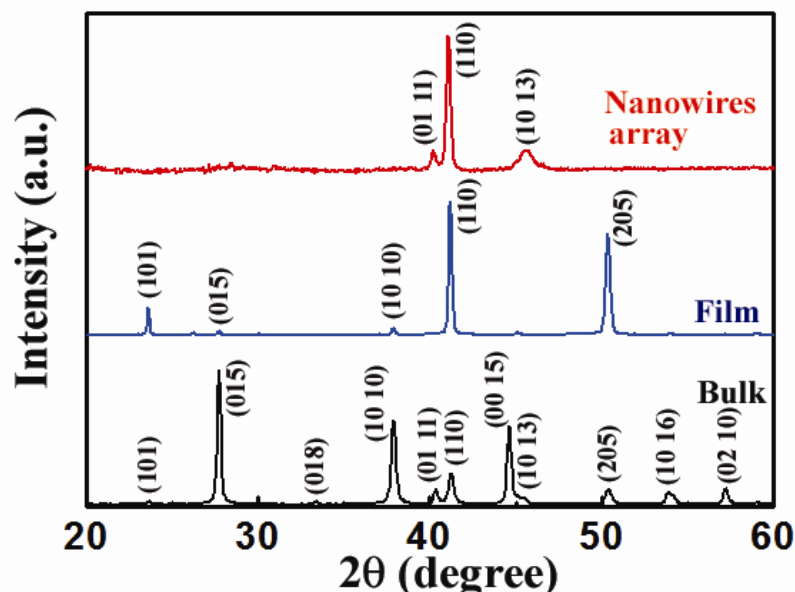


**Figure B1.** X-ray diffraction patterns for  $\text{Bi}_2\text{Te}_3$  bulk, annealed film and as-prepared nanowires array.

X-ray diffraction patterns for  $\text{Bi}_2\text{Te}_3$  bulk, annealed film and as-prepared nanowires array are presented in Figure B1. All peaks can be indexed to those of rhombohedral structure ( $R\bar{3}m$ ), confirming their single-phase purity [12]. The strong (110) peak suggests that the c-axis is parallel to the film surface and perpendicular to the axis of nanowire, respectively. Figure B2 shows the morphology of as-prepared and annealed  $\text{Bi}_2\text{Te}_3$  films. Obviously, annealing yields formation of nanocrystalline structures. The scanning electron micrographs suggest a nucleation-and-growth



mechanism on surface of the substrate. Figure B3a reveals a hexagonally ordered nanochannels in AAM. The approximately 120-nm pore diameter would be then that of  $\text{Bi}_2\text{Te}_3$  nanowires. Figure B3b is a mechanically polished top view of AAM template after being deposited with  $\text{Bi}_2\text{Te}_3$ . Only a few pores remain blank. A same conclusion can be made from the side view in Figure B3c, where most of the pores are filled with  $\text{Bi}_2\text{Te}_3$ . The filling ratio and porosity of the template are estimated to be about 88 % and 25 %, respectively, comparable to the best samples of this kind ever reported [13]. Separated nanowires in Figure B3d were obtained after AAM was dissolved by aqueous NaOH. Most of them have lengths longer than 20  $\mu\text{m}$ . Judging from energy dispersive X-ray analysis, only elements present in both films and nanowires are Bi and Te in the ratio of 0.37: 0.63, corresponding to Te-rich n-type  $\text{Bi}_2\text{Te}_3$ . Extra Te may be situated as substitution to Bi sites or at interstitial sites. They may also be in grain boundaries, but not enough to be observed in XRD as impurity phase [14].

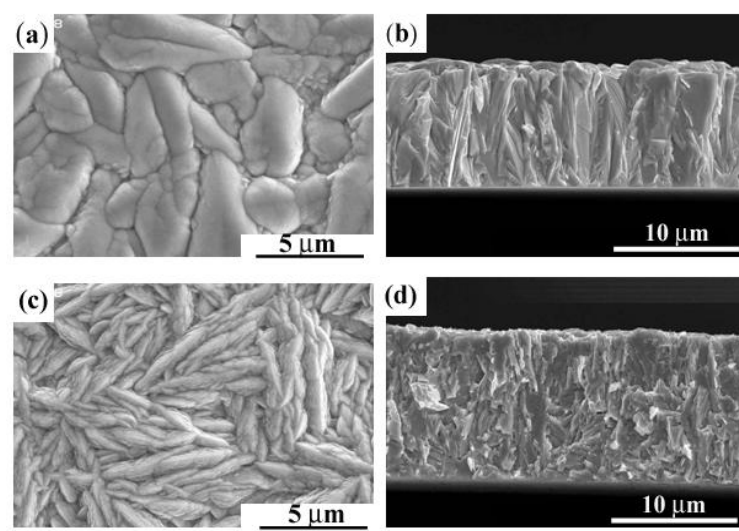


**Figure B2.** Scanning electron micrographs of  $\text{Bi}_2\text{Te}_3$  films: (a) planar and (b) cross-sectional view of as-prepared film, (c) planar and (d) cross-sectional view of annealed film.

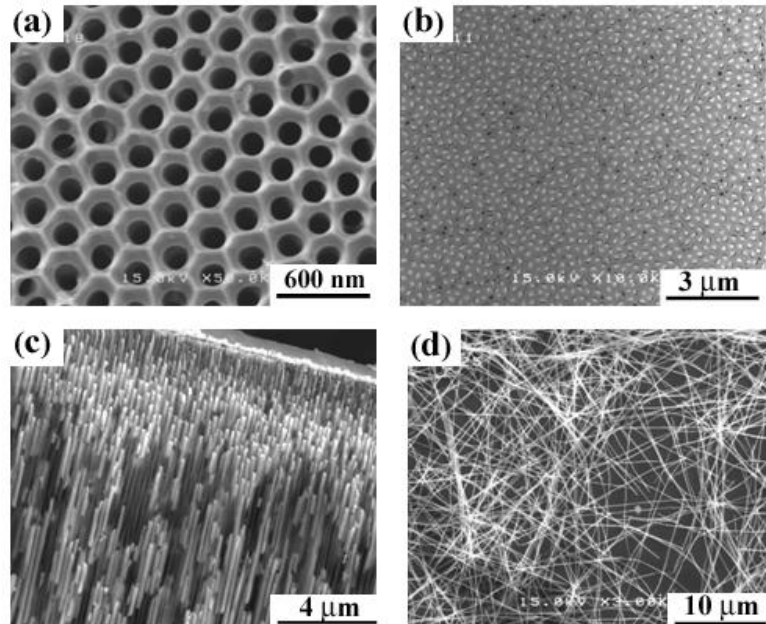


**Figure B3.** Scanning electron micrographs of AAM and  $\text{Bi}_2\text{Te}_3$  nanowires array. (a) Highly ordered nanopores in AAM. (b) Top view of  $\text{Bi}_2\text{Te}_3$  nanowires array. (c) Side view of  $\text{Bi}_2\text{Te}_3$  nanowires array partially embedded in AAM. (d) Separated nanowires after AAM being dissolved.

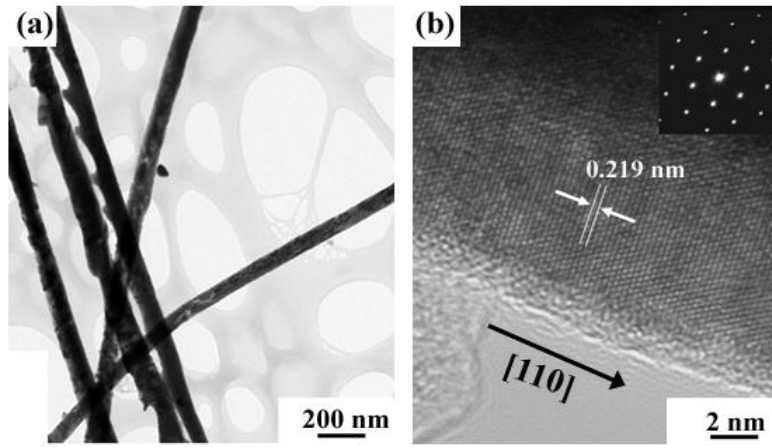


**Figure B4.** (a) TEM image of  $\text{Bi}_2\text{Te}_3$  nanowires. (b) HRTEM image of a single  $\text{Bi}_2\text{Te}_3$  nanowire. Inset: Diffraction patterns of a selected area.

TEM image in Figure B4a reveals the uniform profile of nanowires. A typical high resolution TEM (HRTEM) image of a single  $\text{Bi}_2\text{Te}_3$  nanowire, along with electron diffraction patterns from a selected area, is given in Figure B4b. Lattice fringes yield an inter-planar distance of about 0.219 nm, consistent with the inter-planar spacing of the  $\{110\}$  planes of rhombohedral  $\text{Bi}_2\text{Te}_3$  bulk. This result confirms the direction of the long axis of nanowire is  $[110]$ .

### B3. Properties characterizations

A standard four-probe resistivity measurement was performed on  $\text{Bi}_2\text{Te}_3$  bulk, films and nanowires with a physical property measurement system (Quantum Design). However for nanowires array, gold layers were first deposited on the two sides of array employed as electric contacts of the four-probe method. Measurements of Seebeck coefficient between 120 and 350 K were performed by a longitudinal DC steady-state method on specially designed setups for film (Figure B5a) and nanowires (Figure B5b), with  $S = \Delta V / \Delta T$ , where  $\Delta T$  is the temperature gradient across sample, and  $\Delta V$  the thermo-emf generated by  $\Delta T$ . Typically,  $\Delta T$  is set in the range of 0.5-1 K monitored by a pair of T-type thermocouples. The resulting thermo-emf  $\Delta V$  was continuously recorded by a digital voltmeter. By varying  $\Delta T$ , a statistically averaged  $S$  value was derived from the slope of a  $\Delta V$  vs.  $\Delta T$  plot.

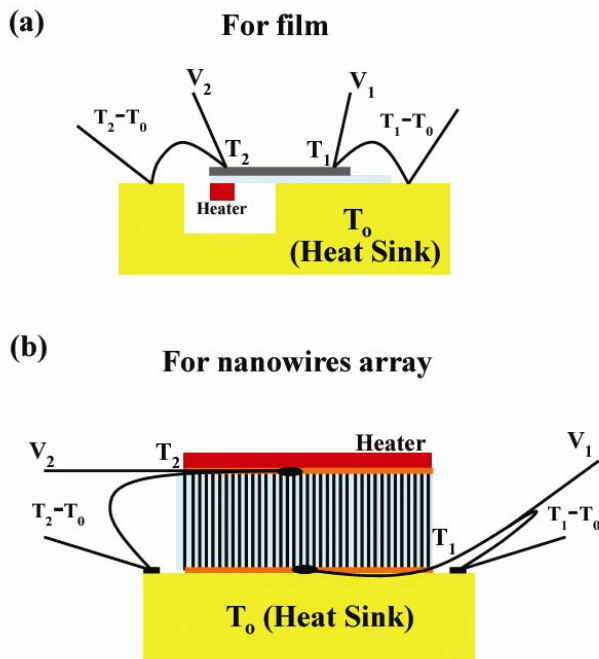


**Figure B5.** Schematic setup for Seebeck coefficient measurements on (a) film and (b) nanowires array in AAM.

Thermal diffusivity measurements were carried out using a laser flash equipment (LFA 457, NETZSCH) on flat disk samples [15]. Briefly described, the front side of specimen was heated by a short pulse of an Nd:YAG laser. The temperature on opposite side was measured by an infrared detector. The measured exothermic curve and laser pulse shape were evaluated by a fitting procedure [16,17]. Before each measurement, a piece of ultra-pure iron (99.999 %) was used as standard to assure the reliability of equipment. A differential scanning calorimeter (Q 100, TA instrument) was employed for heat capacity measurements.

Electrical conductivity  $\sigma$  can be derived from experimentally determined resistivity. The temperature dependence of resistance of nanowires array shows a much larger value than that expected, indicating that most of the nanowires have broken mid-sections inside the template. In order to obtain intrinsic electrical resistivity of nanowires, we set up a measurement on a single nanowire separated from the array at 300K, as shown in the inset of Figure B6a. E-beam lithography and thermal evaporation techniques were applied to fabricate four nickel electrodes onto a 120-nm diameter and 3.7- $\mu\text{m}$  long nanowire. The perfectly linear current-voltage curve in Figure B6a yields a resistance of 1.42 k $\Omega$ . The corresponding resistivity of 4.3  $\mu\Omega\text{-m}$  is smaller than 19  $\mu\Omega\text{-m}$  of stoichiometric bulk  $\text{Bi}_2\text{Te}_3$ . This is somewhat expected for our Te-rich composition. According to Fleurial *et al.*, the electrical resistivity of *n*-type bulk single-crystal  $\text{Bi}_2\text{Te}_3$  decreases towards a low value of 2  $\mu\Omega\text{-m}$  with increasing Te content [18]. Meanwhile, theoretical studies also show that any vacancy, antistructural defects, and substitutional defects will produce higher polarization in bonding between the defect and neighbouring atoms, thereby contribute extra charges to conduction [19,20]. Figure B6b summarizes the temperature dependence of resistivity of each sample between 5 and 350 K. The film has its 300-K resistivity reduced considerably through annealing to 8.3  $\mu\Omega\text{-m}$  from 47.5  $\mu\Omega\text{-m}$  in the highly-disordered, as-prepared condition. It also displays complex temperature dependence, likely reflecting the interplay between semiconducting and semimetallic character. Indeed, even the normally semimetallic  $\text{Bi}_2\text{Te}_3$  in the bulk form can become semiconducting by changing synthesis conditions or relative contents between Bi and Te [21,22]. Furthermore, the highly anisotropic structure could have different electronic and transport behaviors in different directions. Their different temperature dependence could likely contribute to the observed slope change at 200 and again at 50 K.

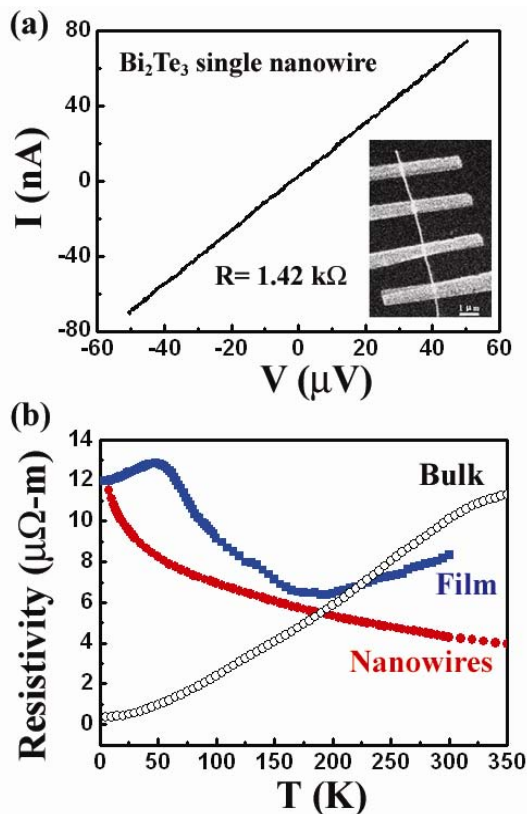


**Figure B6.** (a) I-V curve of single nanowire at 300 K. Inset: SEM image of four-probe setup. (b) Temperature dependence of electrical resistivity for bulk, annealed film and as-prepared nanowires array.

The resistivity of nanowires array plotted in Figure B6b was normalized by the magnitude of single nanowire measured at 300 K. In contrast to the bulk, a semiconducting-type behavior prevails in nanowires array. Its resistivity, along the nanowire axis, follows an exponential temperature dependence. This observation, however, disagrees with theoretical calculations, which result in a positive temperature dependence of resistivity for polycrystalline  $\text{Bi}_2\text{Te}_3$  nanowires [23]. The discrepancy is not surprising, considering the off-stoichiometry and high degree of disorder in the as-prepared nanowires. In fact, such variations in resistivity are often characteristic of nanocrystalline materials, which possess different degrees of disorder and formation of grain boundary barriers in microstructure [24].

Seebeck coefficient data are essential to evaluate thermoelectric materials. Figure B7 shows the temperature dependence of Seebeck coefficients of  $\text{Bi}_2\text{Te}_3$  bulk, annealed films and as-prepared nanowires from 120 to 350 K. The absolute value of  $S$  decreases almost linearly with decreasing temperature, demonstrating diffusive nature of current flow. Comparable results have been previously reported [25].

In the framework of two band model,  $S = (\sigma_e S_e + \sigma_h S_h) / (\sigma_e + \sigma_h)$  [26]. For as-prepared films and nanowires along the nanowire axis,  $S \approx -65 \mu\text{V/K}$  at 300 K, the negative sign points to electrons as majority carriers and the material as a n-type semiconductor. This relatively low value, being less than half of that of bulk, was probably a consequence of structural imperfections and excess Te in electrodeposited, nanocrystalline materials. Structural imperfections caused by anti-site defects [20] and additional Te are able to contribute more carrier concentration. There is often an optimal value of charge carrier density at which Seebeck coefficient is maximum [27]. Higher carrier concentration due to defects would result in a lower Seebeck coefficient. Our electrical resistivity data also suggest that the carrier concentration is likely beyond the optimal value and leads to a lower Seebeck coefficient. Annealing of as-prepared films has been shown to be able in reducing structural defects, as demonstrated by the significant reduction of electrical resistance. However, it raises Seebeck coefficient of films only slightly from -65 to -80  $\mu\text{V/K}$  at 300 K, suggesting that the type of defects critical to  $S$  cannot be simply improved by annealing. Nevertheless, using resistivity and Seebeck coefficient data thus obtained from annealed film, a power factor ( $\sigma S^2$ ) of  $860 \mu\text{W/m K}^2$  at 300 K is derived. This value sits among those of best electrodeposited films. In the as-prepared nanowires, power factor is estimated to be  $\approx 1000 \mu\text{W/m K}^2$ , about 15% superior to that of annealed film.

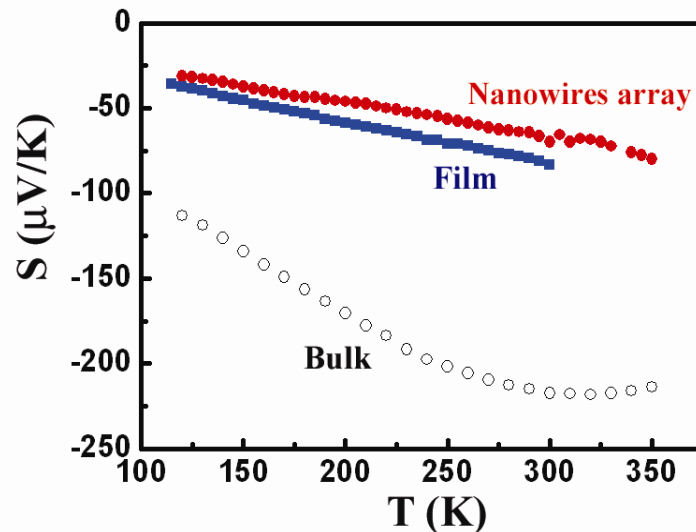


**Figure 7.** Temperature dependence of Seebeck coefficient of  $\text{Bi}_2\text{Te}_3$ : bulk, annealed film and as-prepared nanowires array.

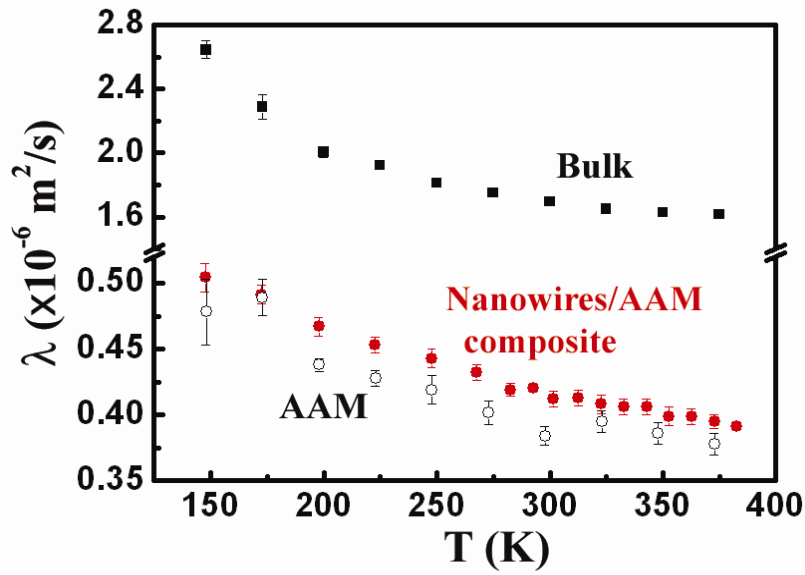


**Figure B8.** Temperature dependence of thermal diffusivity of unfilled AAM and  $\text{Bi}_2\text{Te}_3$ : bulk and nanowires/AAM composite

Instead of direct measurements, thermal conductivity can normally be determined from the relation:

$$\kappa = \lambda \rho C_p$$

where  $\lambda$ ,  $\rho$  and  $C_p$  are thermal diffusivity, density and heat capacity, respectively. In turn, thermal diffusivity was measured using a laser flash apparatus (NETZSCH). The results are summarized in Figure B8. For bulk  $\text{Bi}_2\text{Te}_3$ , the various parameters ( $\lambda = 1.69 \times 10^{-6} \text{ m}^2/\text{s}$ ,  $\rho = 7.70 \text{ g/cm}^3$  and  $C_p = 0.16 \text{ J/g K}$ ) yield  $\kappa = 2.08 \text{ W/m K}$  at 300 K. Similarly, for unfilled AAM template along the channel axis ( $\lambda = 0.38 \times 10^{-6} \text{ m}^2/\text{s}$ ,  $\rho = 3.35 \text{ g/cm}^3$  and  $C_p = 0.77 \text{ J/g K}$ ),  $\kappa = 0.98 \text{ W/m K}$  at 300 K. When it is applied to nanowires/AAM composite along the nanowire axis, a  $\lambda$  of  $0.41 \times 10^{-6} \text{ m}^2/\text{s}$  at 300 K was obtained, which is slightly higher than that of unfilled AAM template, but only about one-fourth of bulk value. Unfortunately, from this result one cannot generate the thermal conductivity of the nanowires alone. To overcome this difficulty, we employ an alternative approach based on a modified effective medium theory model [16,28]. In this model, thermal diffusivity of the composite  $\lambda_{\text{NW+AAM}}$  along the nanowire axis has the following dependence on various parameters of  $\text{Bi}_2\text{Te}_3$  nanowires and AAM, respectively:

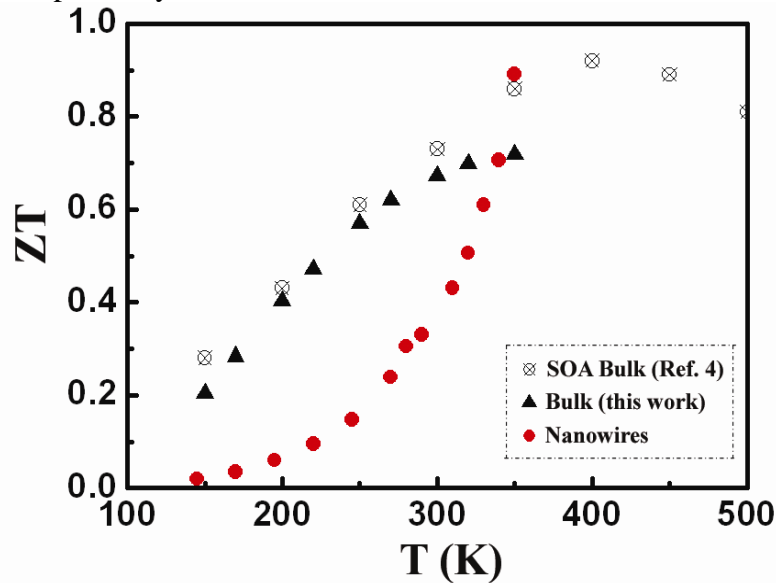


**Figure B9.** Temperature dependence of ZT for nanowires and bulks

$$\lambda_{NW+AAM} = \frac{(1-\Phi) \cdot \kappa_{AAM} + \Phi \cdot \kappa_{NW}}{(1-\Phi) \cdot (\rho C_p)_{AAM} + \Phi \cdot (\rho C_p)_{NW}} \cdot$$

The percentage of nanowire in the composite,  $\Phi \sim 25\%$ , was estimated by the cross-sectional area ratio of the nanowire to the whole composite. The diameter of nanowires ranges between 110 and 135 nm, with an average of about 120 nm. If we assume that nanowires have the same properties as those of bulk, the calculated thermal diffusivity  $\lambda_{NW+AAM}$  of  $0.56 \times 10^{-6} \text{ m}^2/\text{s}$  would obviously be over-estimated as compared to the measured value of  $0.41 \times 10^{-6} \text{ m}^2/\text{s}$  at 300 K. To make the two numbers match, we arrive at a smaller  $\kappa = 0.75 \text{ W/m K}$  for nanowires, which is about one-third of that of bulk. The considerable reductions in thermal conductivity for nanowires were also observed by other groups [29,30]. Then, for a single nanowire with the same  $\kappa = 0.75 \text{ W/m K}$  and a power factor of  $1000 \mu\text{W/m K}^2$ , we estimated the figure of merit  $ZT$  was about 0.45 at 300 K.

Finally, temperature dependence of figure of merit for nanowires between 150 and 375 K in Figure B9 was derived from measured  $S$ ,  $\sigma$  and  $\kappa$  at each given temperature  $T$ . As compared to the state-of-the-art (SOA) bulk  $\text{Bi}_2\text{Te}_3$ , its  $ZT$  monotonically increases with temperature and reaches to a maximum value of 1 at 400 K follows by a decreasing value at higher temperature, it can be seen that the  $ZT$  of nanowires increases dramatically with temperature, and reaches 0.9 at 350 K. It looks like the  $ZT$  can increase to a much higher value if the measurement can be performed at higher temperature.

#### B4. Summary of the results

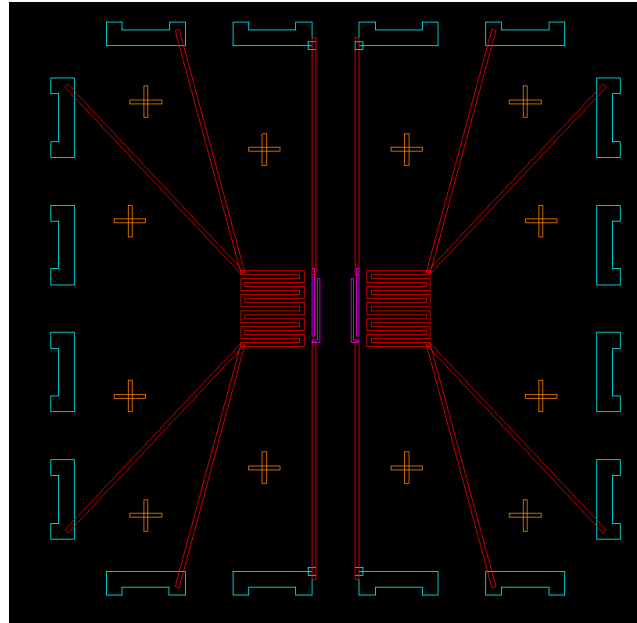


**Figure C1.** The template used for the preparation of the sample for studying thermal rectification effect. The pattern includes contacts and leads for electrical property measurements; and heater for thermal properties characterizations.

Bismuth telluride film and nanowires array (embedded in alumina template) were fabricated by potentiostatically electrodeposition. Both materials are slightly Te-rich, n-type  $\text{Bi}_2\text{Te}_3$ , exhibiting preferred orientation in rhombohedral structure. Their Seebeck coefficient decreases linearly from  $-70 \mu\text{V/K}$  at 300 K with decreasing temperature, showing a diffusive nature of current flow. Electrical resistivity of a single nanowire separated from the array was measured at 300 K, which was then used as reference in determining resistivity of nanowires at other temperatures. Meanwhile, from temperature-dependent thermal diffusivity and heat capacity data, a thermal conductivity value of  $0.75 \text{ W/m K}$  was obtained at 300 K. These parameters subsequently provide an estimated thermoelectric figure of merit  $ZT = 0.45$  at 300 K and likely to reach beyond 0.9 above 350 K, for



$\text{Bi}_2\text{Te}_3$  nanowires. It can be thus concluded that significantly enhanced ZT values can likely be achieved in  $\text{Bi}_2\text{Te}_3$  nanowires at the relatively high temperature region.

### Research approach C—Directional dependent thermal conductivity and thermal rectifier

In order to demonstrate such an effect with a controllable device, we have designed and developed a unique structure to prepare the samples, including the specific template for properties characterizations. Figure C1 shows the lithographic pattern we used in this study. Figure C2 is the fabricated pattern. A tapered feature is used.

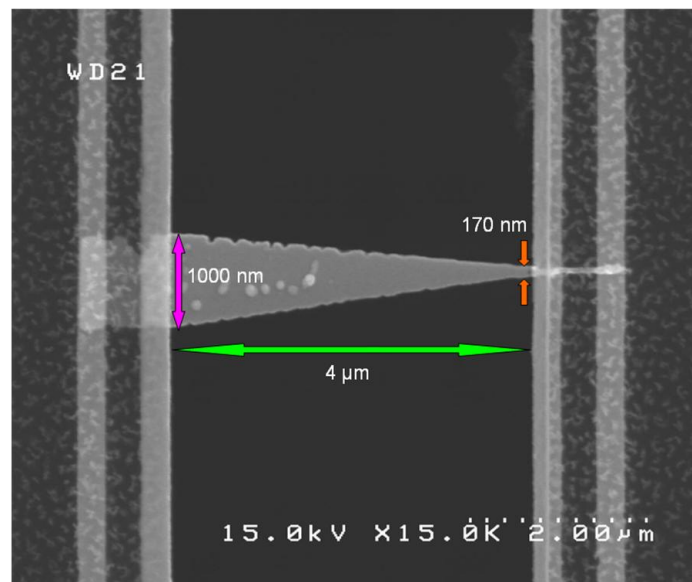


Figure C2. The fabricated asymmetric pattern ( $\text{Bi}_2\text{Te}_3$ ) sample prepared. The width of the narrowest region is  $\sim 170$  nm, the widest region is  $\sim 1000$  nm and the length is  $\sim 4\mu\text{m}$ . It is clearly observed from the SEM image that the edges of the tapered pattern exhibiting zig-zag features.

In order to characterize the properties of the fabricated pattern we need to setup a program to sweep the current with different directions, and then to determine whether there exists any difference. Figure C3a shows the sample pattern with the two heaters made of 10 nm Ni and 50 nm Pt. Figure C3b is the calibrated resistance vs. temperature with the heaters used. Figure C4 displays the schematic of the heat flow needs to be considered and the details how to analyse the thermal characteristics in this special device.

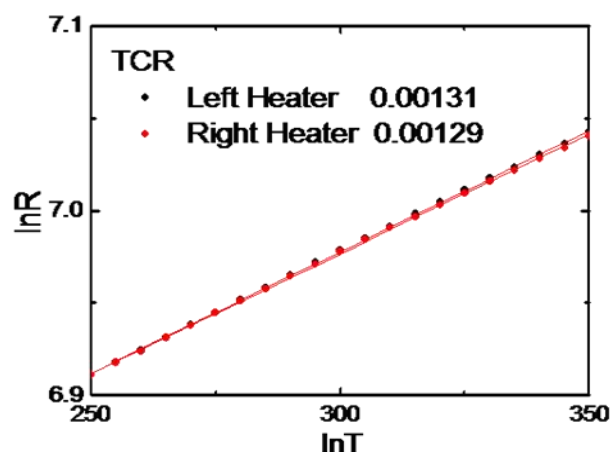
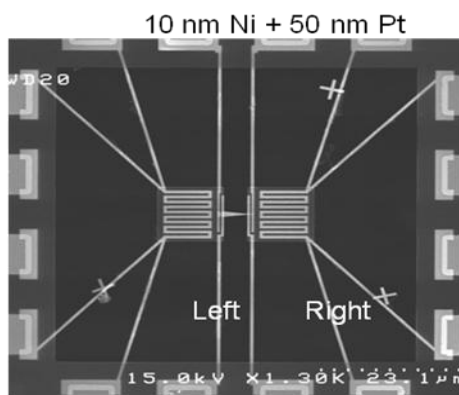
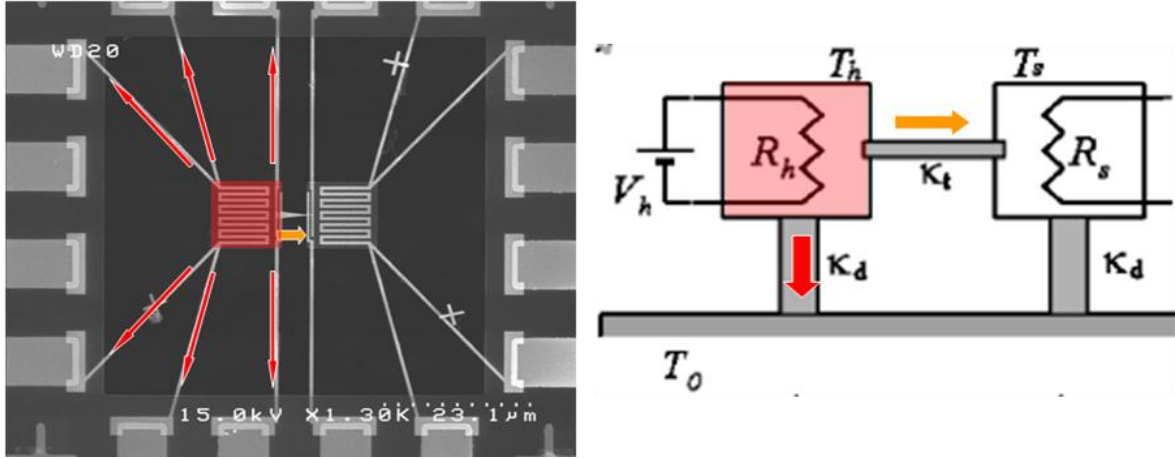
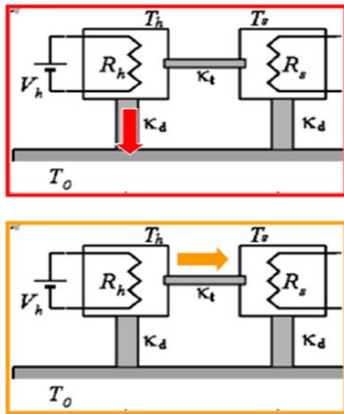


Figure C3. The samples used in this study and the resistance-temperature relation of the heater used.



**Figure C4.** The schematic diagram showing the heat flow in this special device and the parameters to be determined.



#### Thermal conductivity at room temperature

- Platinum (Pt): 69.9 W/m-K
- Nickel (Ni): 76 W/m-K
- Silicon (Si): 83 W/m-K
- $\text{Si}_3\text{N}_4$  : 30 W/m-K

Thermal Conductance  $\kappa_d \sim 1056 \text{ nW/K}$   
(Thermal conductance for each leg  $\sim 176 \text{ nW/K}$ )

Thermal Conductance  $\kappa_t \sim 1060 \text{ nW/K}$   
(Estimated by 500 nm width & 4  $\mu\text{m}$  length)

**Figure C5.** Schematic diagrams the material values used to estimate thermal conductance.

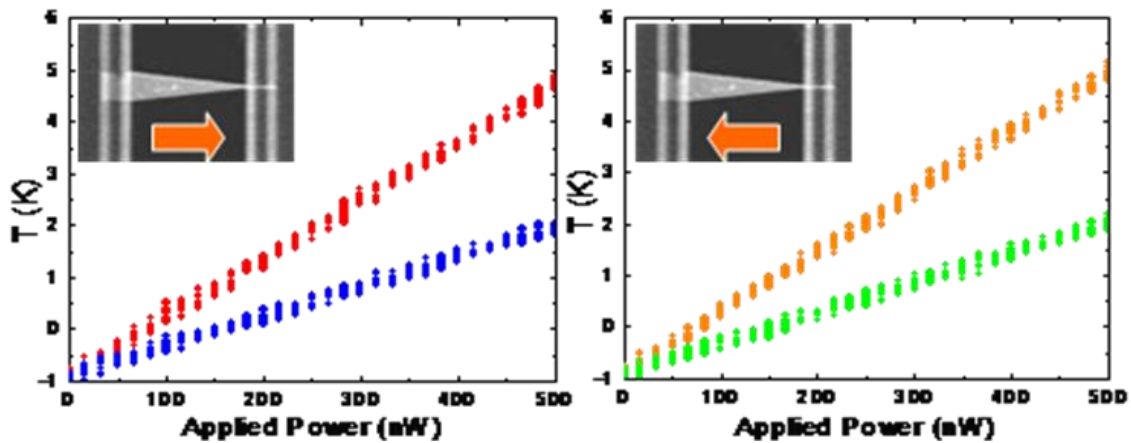


**Figure C6.** The measured temperature vs. applied power of the tapered device. The left panel is the result of heat flows from left region to the right; whereas the right panel is the reverse case.

To evaluate the thermoelectric effect we first need to know the thermal conductance of the device. Consider the system as schetch in figure C4, it is clear that one need first to find out the thermal conductance  $\kappa_t$  and  $\kappa_d$ , which represent the thermal conductance of the tapered structure and the conductance to the heat bath, respectively. Based on the known material parameters, as listed in figure C5, we estimate  $\kappa_t \sim 1060 \text{ nW/K}$  and  $\kappa_d \sim 1056 \text{ nW/K}$ . With these estimated thermal



conductance we are then able to determine the change in temperature by the applied power. The data shown in figure C6 are the results. The two different curves in each panel are the change along  $\kappa_t$  (red—left to right heat flow; or orange—right to left) and  $\kappa_d$  (blue—left to right heat flow or green—right to left) respectively.

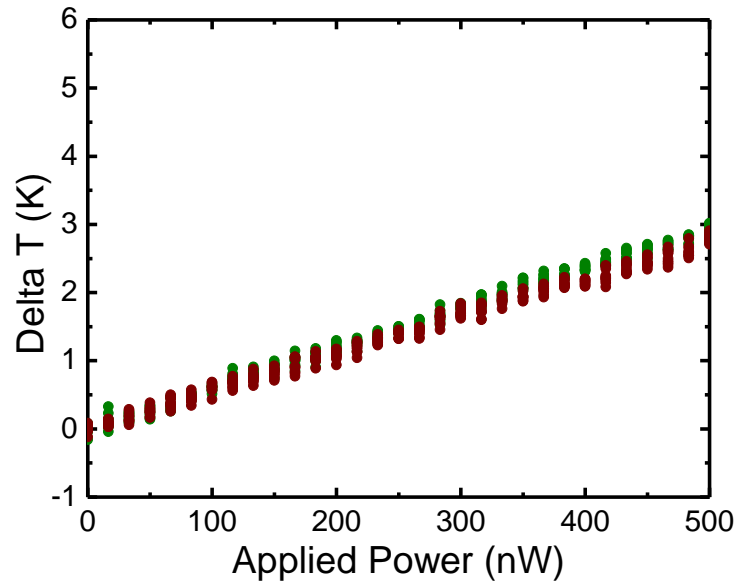


**Figure C7.**  $\Delta T$  versus applied power of the tapered device investigated. The data show the temperature changes in the two directions (left-to-right and right-to-left) are the same within the experimental error.

The final value of the temperature change  $\Delta T$  of the device as a function of the applied power can be summarized in figure C7. We plot in this figure both the changes from left to right and vice versa. The results suggest that the difference in the heat flow in forward and reverse direction is very small. However, we cannot make a conclusive statement that there exists no rectification effect, as the narrowest section in our device is still too big compared with that observed in carbon and boron nitride nanotubes [31].

## REFERENCES

1. Copper Iron Selenide,  $\text{CuFeSe}_2$ , in New Mat Web series, Online Material Data Sheet.
2. Joint Committee on Powder Diffraction Studies, International Centre for Diffraction Data, JCPDS No 81-1959
3. N Hamdadou, M Morsli, A Khelil, J C Bernede. 2006. "Fabrication of n- and p-type doped  $\text{CuFeSe}_2$  thin films achieved by selenization of metal precursors," *J. Phys. D: Appl. Phys.* **39**, 1042–1049
4. Gonzalez-Jimenez F, Jaimes E, Rivas A, D'Orofrío L, Gonzalez J and Quinero M. 1999. "New spin-density waves systems: Cu and Fe selenides and tellurides," *Physica B* **259–261**, 987
5. Lu O, Hu J, Tang K, Deng B, Qian Y and Li Y. 2000. "The synthesis of  $\text{CuFeSe}_2$  through a solventothermal process," *J. Cryst. Growth* **217**, 271
6. Lamazares J, Gonzales-Jimenez F, Jaimes E, D'Onofrio L, Iraldi R, Sanchez-Porras G, Quintero M, Gonzales J, Wooley J C and Lamarche G. 1992. "Magnetic, transport, X-ray diffraction and Mössbauer measurements on  $\text{CuFeSe}_2$ ," *J. Magn. Magn. Mater.* **104–107**, 997
7. D. G. Cahill. 1990. "Thermal conductivity measurement from 30 to 750 K: the  $3\omega$  method," *Rev. Sci. Instrum.* **61**, 802
8. T. Borca-Tasciuc. 2001. "Data reduction in  $3\omega$  method for thin-film thermal conductivity determination," *Rev. Sci. Instrum.* **72**, 2139

9. Martín-González, M. S.; Prieto, A. L.; Gronsby, R.; Sands, T.; Stacy, A. M. *J. Electrochem. Soc.* **2002**, 149, C546.
10. Jessensky, O.; Müller, F.; Gösele, U. *Appl. Phys. Lett.* **1998**, 72, 1173.
11. Yoo, B. Y.; Huang, C.-K.; Lim, J. R.; Herman, J.; Ryan, M. A.; Fleurial, J.-P.; Myung, N. V. *Electrochimica Acta* **2005**, 50, 4371.
12. Mishra, S. K.; Satpathy, S.; Jepsen, O. *J. Phys.: Condens. Matter.* **1997**, 9, 461.
13. Borca-Tasciuc, D.-A.; Chen, G.; Prieto, A.; Martín-González, M. S.; Stacy, A. M.; Sands, T.; Ryan, M. A.; Fleurial, J. P. *Appl. Phys. Lett.* **2004**, 85, 6001.
14. Lan, Y.; Poudel, B.; Ma, Y.; Wang, D.; Dresselhaus, M. S.; Chen, G.; Ren, Z. *Nano Lett.* **2009**, 9, 1419.
15. Parker, W. J.; Jenkins, R. J.; Butler, C. P.; Abbott, G. L. *J. Appl. Phys.* **1961**, 32, 1679.
16. Cape, J. A.; Lehman, G. W. *J. Appl. Phys.* **1963**, 34, 1909.
17. Blumm, J.; Opfermann, J. *High Temp.-High Press.* **2002**, 34, 515.
18. Fleurial, J. P.; Gailliard, L.; Triboulet, R. *J. Phys. Chem. Solids* **1988**, 49, 1237.
19. Pecheur, P.; Toussaint, G. *J. Phys. Chem. Solids* **1994**, 55, 327.
20. Horák, J.; Navrátil, J.; Starý, Z. *J. Phys. Chem. Solids* **1992**, 53, 1067.
21. Augustine, S.; Mathai, E. *Semicond. Sci. Technol.* **2003**, 18, 745.
22. Mansfield, R.; Williams, W. *Proc. Phys. Soc. London* **1958**, 72, 733.
23. Singh, M. P.; Bhandari, C. M. *Solid State Commun.* **2003**, 127, 649.
24. Park, M.-A.; Savran, K.; Kim, Y.-J. *Phys. Stat. Sol. (b)* **2003**, 237, 500.
25. Zhou, J.; Jin, C.; Seol, J. H.; Li, X.; Shi, L. *Appl. Phys. Lett.* **2005**, 87, 133109.
26. Goldsmid, H. J.; Sharp, J. W. *J. Electron. Mater.* **1999**, 28, 869.
27. Snyder, G. J.; Toberer, E. S. *Nat. Mater.* **2008**, 7, 105.
28. Nan, C.-W.; Birringer, R.; Clarke, D. R.; Gleiter, H. *J. Appl. Phys.* **1997**, 81, 6692.
29. Li, D.; Prieto, A. L.; Wu, Y.; Martin-Gonzalez, M. S.; Stacy, A.; Sands, T.; Gronsby, R.; Yang, P.; Majumdar, A. The 21st International Conference on Thermoelectrics: ICT Symposia Proceedings, Long Beach, CA, 25-29, August 2002, p. 333.
30. Moore, A. L.; Pettes, M. T.; Zhou, F.; Shi, L. *J. Appl. Phys.* **2009**, 106, 034310.
31. Chang, C.W., Okawa, D., Majumdar, A., Zettl, A., *Science*, **2006**, 314, 1121

## Publications:

In addition to the works on thermoelectric effect as originally proposed, we have also benefit from this research grant an outstanding research on superconductivity, especially in the area of the newly discovered Fe-based superconductors. The followings are the list of our publications during the period under this grant support.

1. M. N. Ou, S. R. Harutyunyan, S. J. Lai, C. D. Chen, T. J. Yang and Y. Y. Chen, “Electrical and thermal transport in single nickel nanowire”, *Applied Physics Lett*, 92, 063101 (2008).
2. F.C. Hsu, J.Y. Luo, K.W. Yeh, T.K. Chen, T.W. Huang, P.M. Wu, Y.C. Lee, Y.L. Huang, Y.Y. Chu, D.C. Yan, **M.K. Wu**, “Superconductivity in the PbO-type structure  $\alpha$ -FeSe”, *PNAS*, 105, 14262-14264 (2008).
3. K.W. Yeh, T. W. Huang, Y. L. Huang, T. K. Chen, F. C. Hsu, Phillip M. Wu, Y. C. Lee, Y. Y. Chu, C. L. Chen, J. Y. Luo, D. C. Yan, and **M.K. Wu**, “Tellurium substitution effect on superconductivity of the  $\alpha$ -phase Iron Selenide”, *Euro Phys. Letts*, 84, 37002 (2008).
4. K.W. Yeh, H.C. Hsu, T.W. Huang, P.M. Wu, Y.L. Huang, T.K. Chen, J.Y. Luo, **M.K. Wu**, “Se and Te Doping Study of the FeSe Superconductors”, *J. Phys. Soc. Jpn.*, volume 77, p.19-22 (2008).
5. C.L. Chen, K.W. Yeh, D.J. Huang, F.C. Hsu, Y.C. Lee, S.W. Huang, G.Y. Guo, H.-J. Lin, S.M. Rao, and **M.K. Wu**, “Orbital Polarization of the Unoccupied States in Multiferroic  $\text{LiCu}_2\text{O}_2$ ”, *Phys. Rev. B*, 78, 214105 (2008).
6. B.H. Mok, S.M. Rao, M.C. Ling, K.J. Wang, C.T. Ke, P.M. Wu, C.L. Chen, F.C. Hsu, T.W. Huang, J.Y. Luo, D.C. Yan, K.W. Yeh, T.B. Wu, A.M. Chang, **M.K. Wu**, “Growth and investigation of single crystals of the new superconductor  $\alpha$ -FeSe from KCl solutions”, *Crystal Growth & Design*, 9 (7), 3260 (2009).
7. M. J. Wang, J.Y. Luo, T.W. Huang, H. H. Chang, T. K. Chen, F. C. Hsu, C. T. Wu, P. M. Wu, A. M. Chang, **M. K. Wu**, “Crystal Orientation and Thickness Dependence of the Superconducting Transition Temperature of Tetragonal  $\text{FeSe}_{1-x}$  Thin Films”, *Phys. Rev. Letts*. 103, 117002 (2009).
8. P. C. Lee, M. N. Ou, Z. W. Zhong, J. Y. Luo, M. K. Wu and Y. Y. Chen, “The Measurements of Thermal Conductivity of  $\text{CuFeSe}_2$  Thin Film Using  $3\omega$  Technique”, the proceeding of the International Thermal Conductivity Conference (ITCC) and the International Thermal Expansion Symposium (ITES), (2010).
9. C.L. Chen, Y.Y. Chen, S.J. Lin, James C. Ho, P.C. Lee, C.D. Chen, and S.R. Harutyunyan, “Fabrication and Characterization of Electrodeposited Bismuth Telluride Films and Nanowires”, Accepted for publication in *J. Phys Chem C* 2010.
10. C.L. Chen, L.R. Guo, Y.Y. Chen, Y.K. Hwu, C.L. Chang, S.Y. Lee, K.W. Chen, S.J. Lin and J.D. Huang, “In situ real-time investigation of cancer cell photothermolysis mediated by excited gold nanorod surface plasmons”, Accepted for publication in *Biomaterials* 2010.